RSC Advances

PAPER

View Article Online
View Journal | View Issue

Cite this: *RSC Adv.*, 2023, **13**, 22616

Type-II ternary Bi_2WO_6/rGO/$SnFe_2O_4$ heterojunction nanocomposites and their photocatalytic efficiency towards 4-nitrophenol reduction†

Vani Narayanan and Badal Kumar Mandal *

In this study, tin ferrite ($SnFe_2O_4$-spinel) and bismuth tungstate (Bi_2WO_6) encapsulated on reduced graphene oxide (rGO) were synthesised using the hydrothermal method. This heterostructure nanocomposite was characterised using Fourier transform infrared spectroscopy (FT-IR), Ultraviolet-visible spectroscopy (UV-Vis), powder X-ray diffraction (XRD), Scanning electron microscopy (SEM), FT-Raman Spectroscopy (FT-Raman) and X-ray photoelectron spectroscopy (XPS) methods. The powder XRD results showed an increase in lattice parameters and a decrease in size when $SnFe_2O_4$ and Bi_2WO_6 were encapsulated on rGO. The catalytic activity of the type-II ternary Bi_2WO_6/rGO/$SnFe_2O_4$ heterojunction nanocomposite was checked using a model reduction reaction of 4-nitrophenol (4-NP) to 4-aminophenol (4-AP) in the presence of $NaBH_4$ as the reducing agent under light exposure. Bi_2WO_6/rGO/$SnFe_2O_4$ showed better catalytic efficiency than the individual components like $SnFe_2O_4$, rGO/$SnFe_2O_4$, Bi_2WO_6, rGO/Bi_2WO_6 and Bi_2WO_6/$SnFe_2O_4$ nanocomposites. Thus, the type-II ternary Bi_2WO_6/rGO/$SnFe_2O_4$ heterojunction nanocatalyst with better surface area and lower surface energy could be considered as a promising UV-light sensitive catalyst for the detoxification of various environmental pollutants and for other environmental remediations.

Received 31st May 2023
Accepted 19th July 2023

DOI: 10.1039/d3ra03647b

rsc.li/rsc-advances

1 Introduction

Water pollution is one of the top ten problems faced by us in this century. Industrialization was one of the important things that happened to our world as a part of development. Due to industrialization, the growth of industries and factories rapidly increased. Among all the industries textile, pharmaceuticals, and agro-chemical industries are dominant and evident everywhere. As these industries are greater in number, the amount of effluents coming out into the environment is also very large. Due to their poisonous and carcinogenic nature, the excessive presence of organic pollutants such as synthetic dyes, benzene hydrocarbons, sulfonamides, polychlorinated biphenyls (PCBs), phthalates, and aromatic nitro compounds poses major health risks.[1] One of the major pollutants among them is para nitrophenol (4-NP), which is majorly found in industrial effluents.[2] Numerous products, including synthetic colours, rubber, fungicides, pesticides, herbicides, and insecticides, are made using 4-nitrophenol (4-NP) and its derivatives.[3] Many conventional methods are used for the removal of these phenolic compounds, but these methods are not so efficient and cost-effective. The reduction of 4-NP to para-amino phenol (4-AP) by $NaBH_4$ is one of the most efficient and effective methods reported so far. The catalyst would speed up the reduction of 4-NP to 4-AP using $NaBH_4$.[4–6]

The reduction of 4-NP using ferrites has gained much attention in the past few years. Spinel ferrites are composed of transition metal ions and Fe ions, which are distributed on the divalent (tetrahedral) and trivalent (octahedral) sites of the lattice structure, respectively. Their typical formula is MFe_2O_4 (M: Fe, Co, Ni, Mn, *etc.*). Spinel ferrites have been investigated for a variety of applications, including magnetic recording, microwave devices, and biological materials because of their enhanced magnetic and electrical properties.[7] Recently spinel ferrites such as Fe_3O_4,[8,9] $CoFe_2O_4$,[10] $ZnFe_2O_4$,[11] $MnFe_2O_4$,[12] and $NiFe_2O_4$ [13] have been effectively used for the removal of contaminants from water. Among different ferrites, tin-based ferrites have been focused more. $SnFe_2O_4$, which has a face-centered cubic lattice structure, is a typical inverse-spinel. In $SnFe_2O_4$, Fe^{3+} ions are uniformly distributed on the tetrahedron and octahedron sites, whereas Sn^{2+} ions occupy the octahedral sites.[14] $SnFe_2O_4$ has been reported less so far in 4-nitrophenol reduction studies. $SnFe_2O_4$ is a typical p-type semiconductor.[15] The nanostructure of spinel ferrites completely depends on the synthesis conditions used. The crystallinity and magnetic

Department of Chemistry, School of Advanced Sciences, Vellore Institute of Technology, Vellore – 632014, TN, India. E-mail: badalmandal@vit.ac.in

† Electronic supplementary information (ESI) available. See DOI: https://doi.org/10.1039/d3ra03647b

properties of ferrites play a crucial role in their catalytic activities which could be tuned *via* compositing or doping.[16]

One of the simplest Aurivillius oxides that can be easily doped is Bi_2WO_6 having a layered structure with wide physical characteristics that resemble WO_6, a perovskite.[17,18] It has strong oxidising power, better stability, and less band gap which makes them active in visible light. They are also nontoxic in nature which shows high catalytic properties.[18–23] Even though Bi_2WO_6 has better catalytic properties, it is reported that due to its high recombination of photogenerated carriers, it gives low quantum efficiency resulting in reduced catalytic efficiency.[24,25] Because of their smaller size and high surface energy, Bi_2WO_6 shows aggregation issues. This can be overcome by the good dispersion of Bi_2WO_6 on nanosheets. It has been reported that Bi_2WO_6 doped with carbon, nitrogen, and graphene oxide shows better physical and catalytic properties.[26] Among them, graphene oxide-based compositing is preferred due to the two-dimensional layered structure of graphene oxide which enhances their photoinduced charge transfer resulting in improved catalytic activity.[27] Reduced graphene oxide (rGO) is one of the promising materials that can act as a supporting matrix or material with residual oxygen attached to the edges. They are composed of graphene layers with better surface area and low defects. Reduced graphene oxide has a high surface area. Due to this high surface area, it would help to increase the catalytic property.[28,29] In this work, we have focused to composite tin ferrite ($SnFe_2O_4$) and Bi_2WO_6 with rGO to form a ternary nanocomposite. It was synthesised *via* hydrothermal method. The photocatalytic activity of Bi_2WO_6/rGO/$SnFe_2O_4$ was studied using the reduction of 4-nitrophenol to 4-aminophenol using $NaBH_4$ as the reducing agent in an aqueous medium under UV-light exposure.

2 Experimental section

2.1. Chemicals

Graphite powder (crystalline, 50 μm, 99%), Bismuth nitrate pentahydrate (Bi $(NO_3)_3 \cdot 5H_2O$), sodium tungstate dihydrate ($Na_2WO_4 \cdot 2H_2O$) were purchased from Sisco Research Laboratories (SRL). Sodium nitrate ($NaNO_3$) was purchased from Qualigens fine chemicals. Potassium permanganate ($KMnO_4$), hydrogen peroxide (H_2O_2) and Tin chloride ($SnCl_2 \cdot 2H_2O$) were purchased from SD Fine chemicals. Sulphuric acid (H_2SO_4), Ferric chloride hexahydrate ($FeCl_3 \cdot 6H_2O$), and Ammonia (25%) were purchased from Merck, while 4-nitrophenol and hydrazine hydrate were procured from Avra chemicals, Hyderabad-India.

2.2. Synthesis

2.2.1 Synthesis of graphene oxide (GO). Graphene oxide synthesis was done by modified Hummer's method.[30] About 2 g of graphite powder, 2 g of $NaNO_3$ and 90 mL of H_2SO_4 were added to a 1000 mL round bottom flask which was kept in an ice bath condition (temp less than 15 °C) and stirred for 4 h. To the above mixture, 12 g of $KMnO_4$ was added very slowly followed by the addition of 184 mL of distilled water. The mixture was continued to stir in ice bath condition for 2 h followed by another 2 h stirring at room temperature. The above mixture was heated up to 98 °C to obtain a brown-coloured mixture, then reduced to 35 °C and stirred at room temperature for 2 h. To this mixture, 40 mL of H_2O_2 was added very slowly to obtain a green-coloured solution. The above mixture was equally separated into two 500 mL beakers and 200 mL distilled water was added separately to each beaker. This solution was stirred at room temperature for 1 h and kept overnight to settle down the residue formed. The residue was collected by centrifugation and washed using 10% HCl to make the pH neutral. The residue was then dried at 80 °C and pulverized to obtain GO powder.

2.2.2 Synthesis of reduced graphene oxide (rGO). 320 mg of powdered graphene oxide (GO) synthesised *via* modified hummer's method were well dispersed in 120 mL of distilled water using ultrasonication method. Then 32 μL of hydrazine hydrate was added to the suspension and transferred into a 100 mL Teflon reactor and it was then kept at 180 °C for 18 h reaction. The black-coloured precipitate was collected, washed several times, dried at 80 °C, and pulverized to get rGO.

2.2.3 Synthesis of rGO/$SnFe_2O_4$. 100 mg of powdered rGO was well dispersed in 100 mL of distilled water. To the above solution, 1.2 g of $FeCl_3 \cdot 6H_2O$ and 0.8 g of $SnCl_2 \cdot 2H_2O$ were added and stirred until the metals salts dissolves completely. This mixture was heated up to 80 °C and 10 mL of ammonium hydroxide (2 M) solution was added dropwise to adjust pH to 10. Then the precipitate formed was centrifuged and washed several times with an ethanol–water mixture to remove the impurities and dried at 80 °C followed by pulverizing to get the powder sample.

2.2.4 Synthesis of Bi_2WO_6/rGO/$SnFe_2O_4$. 50 mg of synthesized rGO/$SnFe_2O_4$ was well dispersed in 50 mL of distilled water. Then 9.0 mg of sodium tungstate dihydrate ($Na_2WO_6 \cdot 2H_2O$) and 26.7 mg of bismuth nitrate pentahydrate $(Bi(NO_3)_2) \cdot 5H_2O$ were added to the above solution and stirred continuously for 5–6 h. Then the mixture was transferred into a Teflon reactor and kept at 180 °C for 12 h to form Bi_2WO_6/rGO/$SnFe_2O_4$. The formed precipitate was centrifuged and washed thoroughly with ethanol–water mixture to remove the impurities and then dried at 80 °C followed by pulverizing to get the fine powders. This powder was calcined at 700 °C for 3 h at a ramp temperature of 4 °C min^{-1} to get Bi_2WO_6/rGO/$SnFe_2O_4$ nanocomposite. Similarly, $SnFe_2O_4$ and Bi_2WO_6/$SnFe_2O_4$ were also synthesised following the same procedure without rGO. The schematic diagram for facile hydrothermal synthesis of type-II ternary Bi_2WO_6/rGO/$SnFe_2O_4$ heterojunction nanocomposite is shown in Scheme 1.

3. Catalytic activity

The catalytic activity of the prepared nanocomposites was done by the reduction of 4-nitrophenol to 4-aminophenol with $NaBH_4$ as the reducing agent under a light source. 50 mL of 4-NP (0.0001 M) was taken in a beaker and 0.01 M of $NaBH_4$ and the required amount of catalyst were added and magnetically stirred in the dark condition for 10 minutes to obtain the adsorption/desorption equilibrium. Then the above mixture was transferred to photoreactor quartz tubes and kept under

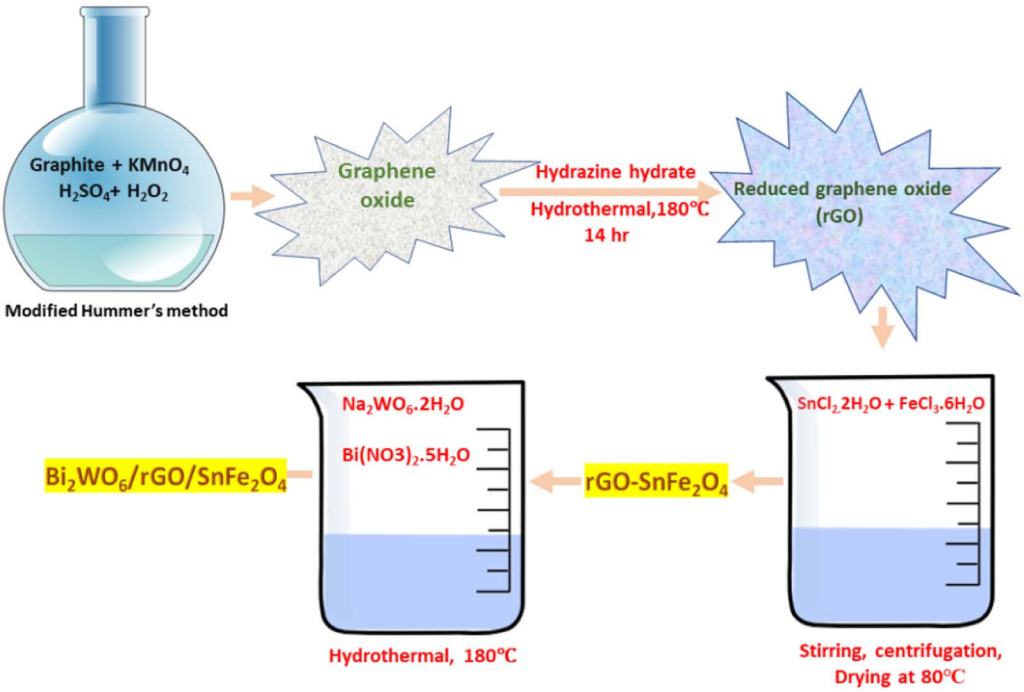

Scheme 1 The schematic diagram for the synthesis of type-II ternary Bi_2WO_6/rGO/$SnFe_2O_4$ heterojunction nanocomposite by hydrothermal method.

UV-light irradiation. 1 mL of the mixture was taken before irradiation of UV-light and after every 10 min interval samples were collected, centrifuged and analysed using UV-Vis spectroscopy at λ_{max} of 365 nm. The below-mentioned formula was used to determine the catalytic efficiency of the nanocomposites for the reduction of 4-nitrophenol to 4-aminophenol.

$$\eta = \frac{C_0 - C_f}{C_0} \times 100$$

where C_0 is the initial concentration of 4-NP and C_f is the final concentration of 4-NP at time t, η is catalytic efficiency in percentage.

4. Characterization

Material characterizations were done using X-ray diffraction methods (XRD-Bruker D8 advance), Fourier transform infrared spectroscopy (FT-IR-Shimadzu IR affinity-1), UV-visible spectrophotometer (Jasco V-670 PC), Scanning electron microscopy (SEM-Carl Zeis EVO/18 research), field emission scanning electron microscopy (FE-SEM-Thermo Fischer Quanta 250 FEG), thermogravimetric analysis (TGA-TA instruments USA, SDT Q600), X-ray Photoelectron spectroscopy (Omicron Nanotechnology Ltd, Germany). Photocatalytic reactions were carried out using a photoreactor (Heber-visible annular type photoreactor).

5. Results and discussion

5.1 Powder XRD analysis

Powder XRD analysis was done to know the phase purity and crystallinity of the catalyst prepared. It helps to determine the orientation of a single crystal or grain and measures the average distances between layers or rows of atoms.[31] Fig. 1 shows the powder XRD patterns of GO, rGO, $SnFe_2O_4$, rGO/$SnFe_2O_4$, Bi_2WO_6, Bi_2WO_6/rGO/$SnFe_2O_4$. Fig. 1a is the XRD pattern of GO synthesised *via* modified Hummer's method and rGO using hydrazine hydrate as the reducing agent. The sharp peak at 10.2° indicates the complete and successful oxidation of graphite into GO followed by oxidation and exfoliation. It is evidence of an increase in *d*-spacing value from 0.34 nm to 0.82 nm.[31] After reduction using hydrazine hydrate the 2θ value of GO has shifted to 24.4° which confirms the complete reduction of GO to rGO. The XRD peaks of individual binary composites are also well matched with the standard ref. 30. In Fig. 1b the broadened peak of $SnFe_2O_4$ from the lattice plane (222) represents the monophasic inverse spinel structure which shows a lattice constant like that of Fe_3O_4. The diffraction peaks of $SnFe_2O_4$ are much better after calcination at 700 °C and above which could be due to an increase in crystallite size and a decrease in lattice parameters. The peaks with *hkl* values of (220), (222), (511), (440), (442) given in Fig. 1b are the characteristic peaks of $SnFe_2O_4$ which match with the JCPDS data card no of JCPDS-01-071-0695. When it comes to rGO/$SnFe_2O_4$, there is a slight shift in the characteristic peaks of $SnFe_2O_4$. But no impurity phases are observed, which means the introduction of rGO and high-temperature calcination does not affect the crystal structure of $SnFe_2O_4$.[32] We can observe the main peak of rGO at 25° and other characteristic peaks of $SnFe_2O_4$ with a slight red shift in peaks of rGO/$SnFe_2O_4$. This slight peak shift could be due to change in particle size and crystallinity after calcination. The particle sizes were calculated using Scherrer's

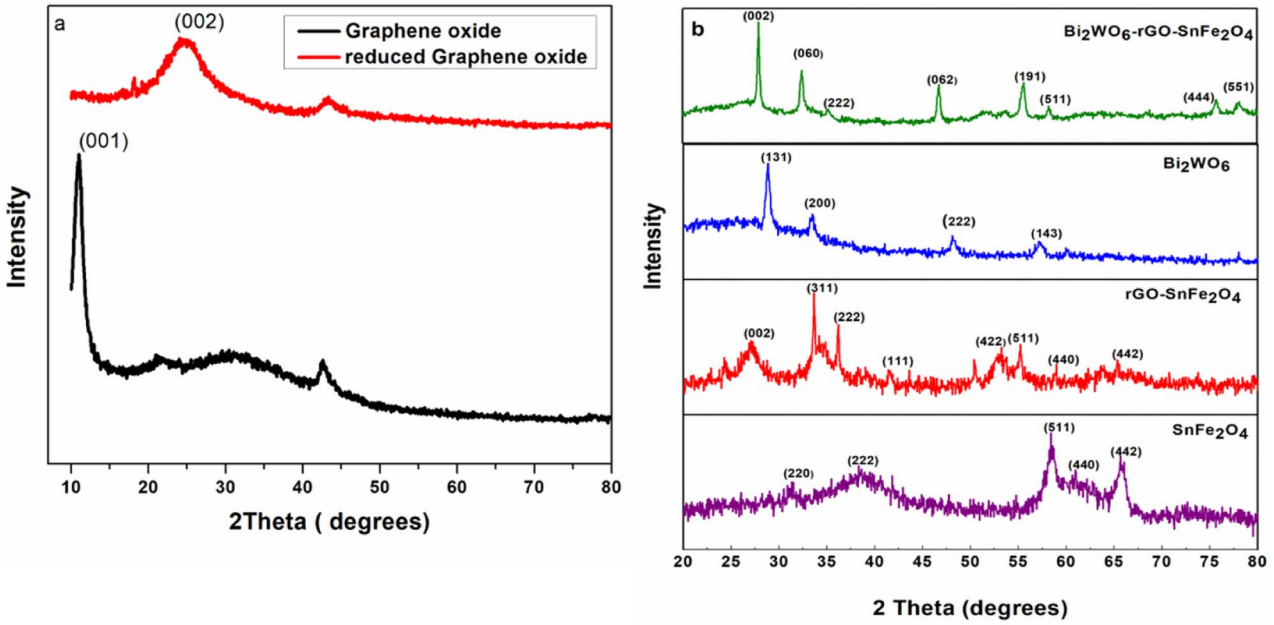

Fig. 1 Powder XRD patterns of (a) GO and rGO, (b) $SnFe_2O_4$, rGO/$SnFe_2O_4$, Bi_2WO_6 and Bi_2WO_6/rGO/$SnFe_2O_4$.

equation. Sharp and crystalline peaks are observed in the Bi_2WO_6 XRD diffractogram. The peaks at *hkl* values of (131), (200), (222), and (143) are the characteristic peaks of Bi_2WO_6 that matches with the JCPDS data card no of JCPDS-01-079-2381. In the final ternary nanocomposite both the characteristic peaks of Bi_2WO_6 and $SnFe_2O_4$ are seen, but the intensity of Bi_2WO_6 and rGO peaks are diminished which could be due to the interaction of Bi_2WO_6 with rGO/$SnFe_2O_4$. The lattice parameter of the catalysts was calculated using the formula given below as

$$a = [h^2 + k^2 + l^2]^{1/2}$$

where, h, k and l are Miller indices, d is the inter-planar distance and a is the lattice parameter. In addition, the average crystallite size was calculated using the given below formula.[33]

$$D = k\lambda/(\beta \cos \theta)$$

where, D is the average crystallite size, λ is the X-ray wavelength, β is the full width at half maximum (FWHM) and θ is the Bragg's angle. Lattice parameters of each peak of the final catalyst (Bi_2WO_6/rGO/$SnFe_2O_4$) and average crystallite sizes are given in Table 1.

5.2 FT-IR analysis

FT-IR analyses were used to get the infrared spectrum of the catalysts synthesised. It helps to identify the functional groups and various types of bonding present in the compound. Fig. 2a and b is the FT-IR spectra of GO, rGO, and various catalysts synthesised. Both GO and rGO have an almost similar spectrum. The peak at 1037.63 cm^{-1} corresponds to the C–O group which confirms the complete oxidation of graphite to GO. The peak between 1600 cm^{-1} and 1700 cm^{-1} corresponds to the C=C bond which is one of the prominent peaks in GO. A broad peak between 2800 cm^{-1} and 3800 cm^{-1} is due to the O–H stretching peak of water molecules. All these peaks confirm the formation of GO and rGO. In Fig. 2b the peaks between 500 and 600 cm^{-1} could be due to the stretching vibrational modes of Fe–O and Bi–O. The narrow peaks within 700–800 cm^{-1} shows the W–O stretching.

5.3 Optical studies

UV-DRS analyses were carried out to understand the optical properties of the catalysts prepared. Based on Kubelka–Munk theory, the equation given below helps to interpret the spectra by combining reflectance data and the absorption coefficient.

$$\alpha h\nu = A(h\nu - E_g)^{n/2}$$

where, α: absorption co-efficient, h: Planck's constant, ν: light frequency, E_g: Band gap, A: proportionality constant.[34] On

Table 1 Lattice parameters and crystallite sizes of type-II ternary Bi_2WO_6/rGO/$SnFe_2O_4$ heterojunction nanocomposite

Peaks	Lattice parameters (Å)	Crystallite size (nm)
002	6.56	28.5
060	16.38	24.5
222	8.59	19.4
062	12.23	14.3
191	15.04	14.5
511	8.59	11.1
444	8.59	10.5
551	8.60	10.2

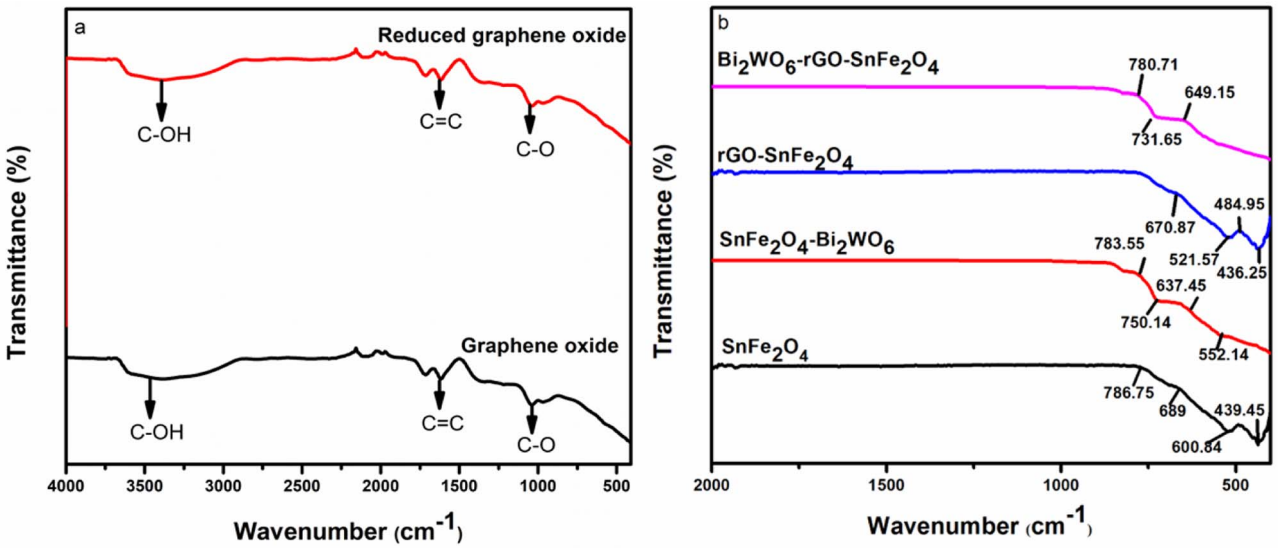

Fig. 2 FT-IR spectra of (a) GO and rGO, (b) $SnFe_2O_4$, $SnFe_2O_4$–Bi_2WO_6, rGO-$SnFe_2O_4$, and Bi_2WO_6-rGO-$SnFe_2O_4$.

extrapolation of the plot $(\alpha h\nu)^2$ *versus* energy the band gap energy of the materials synthesised were calculated. Fig. 3a is UV-DRS plot of Bi_2WO_6/rGO/$SnFe_2O_4$.The wider peak at higher wavelength shows that the ternary composite can be activated at visible light region. Fig. 3b and S1–S5 in the ESI† are the Tauc plots that give the band gap energy of each catalyst prepared. Based on Tauc plot results, the band gap energies of $SnFe_2O_4$, rGO/$SnFe_2O_4$, Bi_2WO_6, rGO/Bi_2WO_6 Bi_2WO_6/$SnFe_2O_4$, and Bi_2WO_6/rGO/$SnFe_2O_4$ are 1.5 eV, 1.5 eV, 1.8 eV, 1.4 eV, 1.67 eV and 1.27 eV respectively.[24,25] GO and rGO has band gap energies of 1.6–2.5 eV and 1.1–1.4 eV. Here type-II heterojunction Bi_2WO_6/rGO/$SnFe_2O_4$ is showing the least band gap energy which could be due to the interaction of Bi_2WO_6 with $SnFe_2O_4$ with the help of rGO *via* compositing, where rGO acts as a matrix to enhance light adsorption capacity in the visible light region with a redshift.

5.4 Morphological studies

SEM analysis were done to understand the surface morphology of the catalysts prepared. Fig. 4a–c show the SEM micrographs and EDX spectra of GO and rGO and Bi_2WO_6/rGO/$SnFe_2O_4$. In the GO micrograph we can see a wrinkled and layered flake-like structure which confirms the complete oxidation of graphite to GO,[35] whereas in rGO crumbled layered flakes in a disordered arrangement can be seen which could be due to reduction by hydrazine hydrate which matches with the results published.[36] Fig. S6† shows that the synthesised $SnFe_2O_4$ *via in situ* preparation method has a spherical morphology on the surface. The SEM micrograph of rGO/$SnFe_2O_4$ (Fig. S7†) shows spherical structures of $SnFe_2O_4$ on layered flakes of rGO. The SEM micrograph of Bi_2WO_6 (Fig. S8†) shows spherical structures of Bi_2BO_6. Zhang *et al.* (2016) reported that Bi_2WO_6 also possesses well defined spherical structure on the surface.[37] The SEM

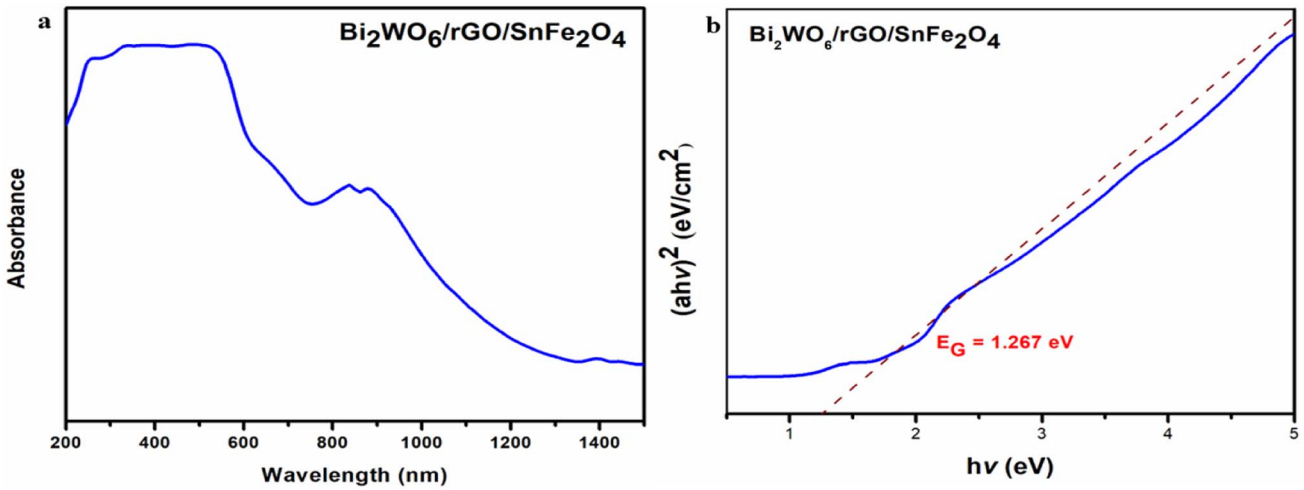

Fig. 3 (a) UV-DRS absorption spectrum of Bi_2WO_6/rGO/$SnFe_2O_4$, (b) Tauc-plot for band gap calculation energy of the composite Bi_2WO_6/rGo/$SnFe_2O_4$.

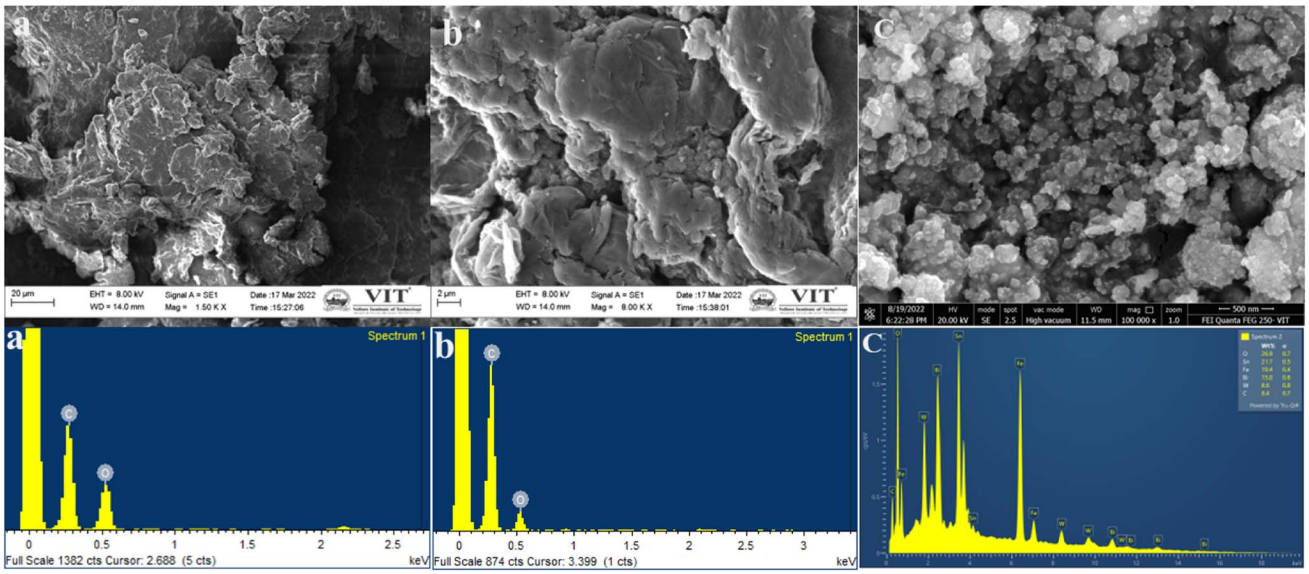

Fig. 4 SEM-EDX images of (a) GO, (b) rGO and (c) Bi_2WO_6/rGO/$SnFe_2O_4$.

micrograph of Bi_2WO_6/rGO/$SnFe_2O_4$ (Fig. 4c) shows more spherical structures on layered flakes of rGO which could be due to Bi_2WO_6 and $SnFe_2O_4$. This confirms that no structural damages occurred on rGO after compositing with Bi_2WO_6 and $SnFe_2O_4$. The EDAX also confirms the presence of all elements.

5.5 XPS analysis

To confirm the presence of all elements and valence states of them XPS analysis were carried out. The full scan survey spectrum shows the peaks of Sn, Fe, Bi, W, O, and carbon (Fig. 5a). In the Bi spectrogram the peaks at binding energies of 160.31 eV and 163.50 eV correspond to Bi $4f_{7/2}$ and Bi $4f_{5/2}$ doublet which confirms the presence of Bi^{3+} (refs. [38] and 39) (Fig. 5b). In the spectrogram of W, the peaks at binding energies of 36.43 eV and 38.56 eV show the peaks of $4f_{7/2}$ and W $4f_{5/2}$ doublet which proves that tungsten exists in the W^{+6} oxidation state in the nanocomposite[40] (Fig. 5c). The O 1 s spectrogram shows a peak at a binding energy of 530.35 eV which indicates the Sn–(Fe)–O bonding (Fig. 5d). In the spectrum of Sn 3d

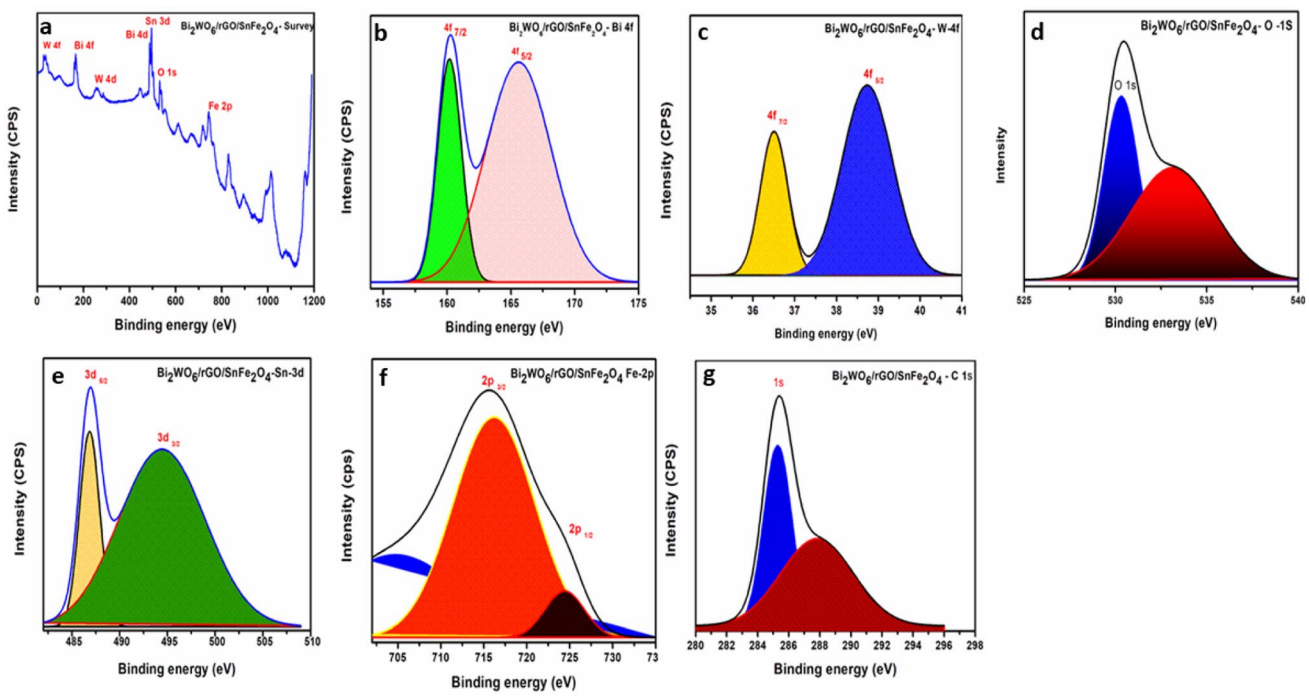

Fig. 5 XPS spectra of (a) total survey, (b) Bi 4f, (c) W 4f, (d) O 1s, (e) Sn 3d, (f) Fe 2p, (g) C 1s.

region (Fig. 5e), the two prominent peaks with binding energies of 486.83 eV and 494.95 eV represent the Sn $3d_{5/2}$ and Sn $3d_{3/2}$ doublet which suggests that Sn exist in Sn^{2+} state.[41] In Fe 2p (Fig. 5f) spectrogram, the peaks at binding energies of 710.10 eV and 723.02 eV matches with the Fe $2p_{3/2}$ and Fe $2p_{1/2}$ doublet which confirms the presence of octahedral and tetrahedral sites of Fe^{3+} of spinel ferrite[42] (Fig. 5g). The peak of C 1s at a binding energy of 284.24 eV represents the C–C/C–H bond.[43] All these data confirm the presence of all elements in the ternary nanocomposite with the predicted oxidation sates and thus the successful formation of Bi_2WO_6/rGO/$SnFe_2O_4$ nanocomposites was finalised. Table 2 summarises the valence states of each element obtained through XPS with respect to literature.

5.6 Thermal studies

Thermogravimetric analysis (TGA) was done to know the thermal stability of the synthesized nanocomposite *i.e.* the changes in weight of the composite with respect to temperature differential thermal analysis (DTA) helps to know the type of changes that a sample undergoes on temperature variation and it also determines the change in temperature between a reference object and a sample during a heat-up or cool-down. The airflow rate maintained in TGA analysis was 100 mL min^{-1} and the temperature of the reactor was increased at a rate of 20 °C min^{-1}. The testing range of temperature was from room temperature to 800 °C. Fig. 6a and S9† shows the TGA and DTA plots of the catalyst Bi_2WO_6/rGO/$SnFe_2O_4$. In Fig. 6a it shows a steady decrease in weight percentage with respect to the temperature till 95 °C with a weight loss of 8.71% which could be due to desorption of water molecules from the surface of the catalyst. From the temperature 95 °C till 525 °C we can observe another slow and steady decrease in weight percentage with a final weight loss of 10.42%. This decrease of weight percentage at 525 °C could be due to the removal of organic materials, adsorbed water molecules, and due to defect formation. This removal of hydroxyl ions from the catalyst surface would be followed by crystallisation process.[44] It is clear that there is no decomposition of substance is noticed above 550 °C with almost nil weight loss. So the calcination temperature of the prepared catalyst was fixed at 700 °C in this study. The DTA graph (Fig. S9†) shows a deep endothermic peak at 80.39 °C followed by a broad oxidation (exothermic) curve from 300 °C to 500 °C.

5.7 Surface area analysis

BET analysis was done to know the N_2-adsorption–desorption isotherm of Bi_2WO_6/rGO/$SnFe_2O_4$.The ternary heterojunction

Table 2 XPS analysis results: spin–orbit splitting and valence states of elements present in the synthesized nanomaterial

Element	Spin orbit splitting	Valence state	References
Tin (Sn)	$3d_{5/2}$, $3d_{3/2}$	+2	38
Iron (Fe)	$2p_{3/2}$, $2p_{1/2}$	+3	39
Tungsten (W)	$4f_{7/2}$, $4f_{5/2}$	+6	41
Bismuth (Bi)	$4f_{7/2}$, $4f_{5/2}$	+3	42 and 43

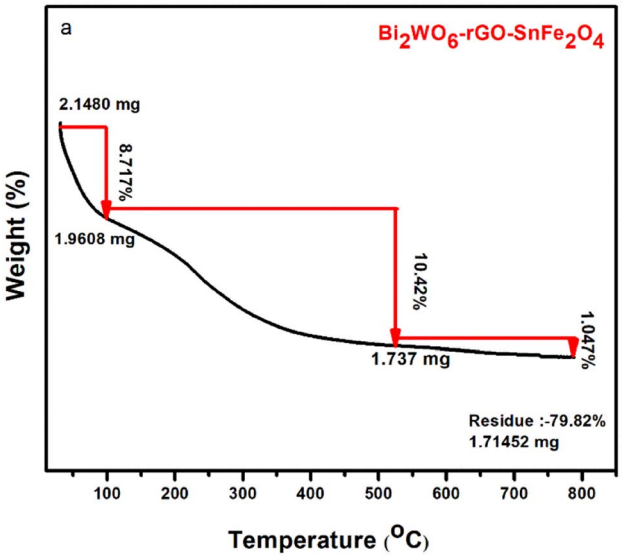

Fig. 6 Thermogravimetric analysis of the catalyst Bi_2WO_6/rGO/$SnFe_2O_4$.

exhibits a typical type IV isotherm with a better adsorption capacity and high relative pressure (P/P_0 > 0.6). This gives an evident picture of existence of abundant meso and macropores on the surface of the composite (Fig. 7). The pore size distribution curve Fig. S10† shows a sharp peak at 26.9 nm which indicates the mesoporous nature of the pores present on the surface of the ternary nanocomposite.

5.8 Raman spectroscopy

Raman spectral analysis was done to know the structural changes and defects present in the catalyst. Fig. 8 is the Raman spectrum of the composite Bi_2WO_6/rGO/$SnFe_2O_4$. The Raman analysis was done in the wavenumber range of 50 cm^{-1} to

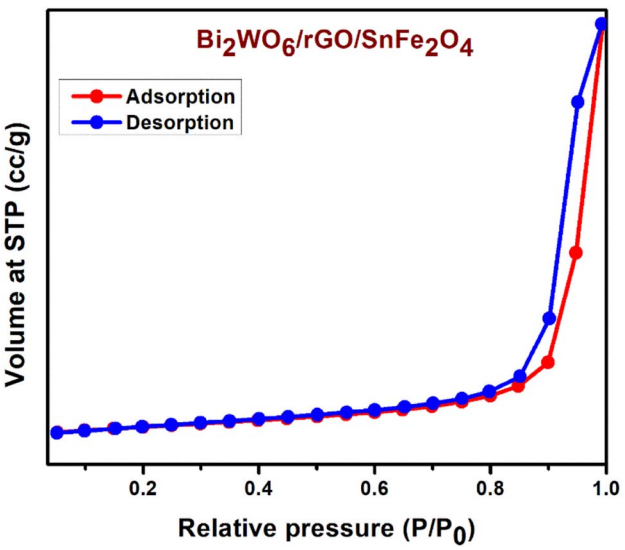

Fig. 7 BET graph of Bi_2WO_6/rGO/$SnFe_2O_4$.

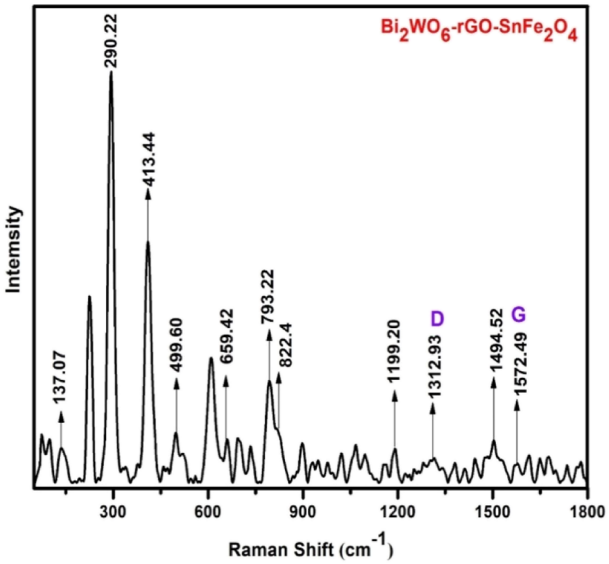

Fig. 8 Raman spectrum of ternary Bi_2WO_6/rGO/$SnFe_2O_4$ heterojunction nanocomposite.

1800 cm^{-1}. The strong peaks at 822.4 cm^{-1} and 793.22 cm^{-1} correspond to the symmetric and antisymmetric stretching vibrational modes of O–W–O. The appearance of a small peak between 690 cm^{-1} and 750 cm^{-1} represents the asymmetric bridge mode of WO_6. A sharp peak at 413.44 cm^{-1} stands for the asymmetric bending vibration of Bi–O. The small peaks below 150 cm^{-1} are basically due to the transitional movement of W^{6+} and Bi^{3+}.[45,46] All carbon structures exhibit the G-band which is produced by C–C stretching, and the D-band due to structural defects. The peak intensity of D band and G band decreased due to the reduction process of graphene oxide.[47] The ID/IG ratio is found to be 1.3138 which means rGO is formed with better defects. The peaks at 499.60 cm^{-1} and 659.42 cm^{-1} are the prominent fingerprint peaks for Sn–Fe–O vibrations.[48] Since all the peaks matched with the reported literature the structure and vibrational modes of the catalyst prepared were confirmed.

5.9 Photocatalytic reduction study

The formation of the band structure is another important factor of a catalyst to know the catalytic activity of the photocatalyst. The conduction band edge potential (E_{CB}) and valence band edge potential (E_{VB}) of both $SnFe_2O_4$ and Bi_2WO_6 were found separately using the formula given below.[49]

$$E_{CB} = X - E_e - 0.5E_g \text{ and } E_{VB} = E_{CB} + E_g$$

where X is the electronegativity of the semiconductor; E_e is the free energy of electrons according to the hydrogen scale (4.5 eV); E_g is the band gap energy of the semiconductor. Using this band gap energy values the conduction band edge potential (E_{CB}) and valence band edge potential were found separately. $SnFe_2O_4$ and Bi_2WO_6 have 0.1926 eV, 2.3926 eV as the E_{CB} and the E_{VB} of $SnFe_2O_4$ and Bi_2WO_6 are 0.75 eV, 2.65 eV. Hence, $SnFe_2O_4$ has low E_{CB} and E_{VB} compared to Bi_2WO_6. Thus it is considered as semiconductor 1 and Bi_2WO_6 as semiconductor 2 in the ternary nanocomposite and rGO will act as a supporting matrix to hold the tin based spinel and Bi_2WO_6 which also enhances the catalytic activity of the catalyst. Based on this band structure arrangement movement of electrons and other charge-carrying species would be easier and degradation process would be more feasible.

Nitrophenol may present in its different isomers (*ortho*, *meta* and *para* nitrophenol), but 4-NPs are widely seen in industrial effluents. The exposure to 4-NP and 4-AP causes various health issues fervescence, cyanosis, methemoglobinemia, and liver and kidney damage. On comparing the toxicity level of 4-NP and 4-AP, the LD_{50} (lethal dosage) value of 4-NP is 202 mg kg^{-1} BW (rats) while it is 282 mg kg^{-1} BW (mice)[50] and that of 4-AP is 375 mg kg^{-1} BW (rats).[51] Since the LD_{50} of 4-AP is higher than that of 4-NP, it is considered to be less toxic in nature. Thus the photocatalytic property of the ternary heterojunction nanocomposite was studied through the model reaction of 4-NP reduction to 4-AP using $NaBH_4$ as the reducing agent in the presence of UV-light at 365 nm. Although all three nanomaterials are visible light active, Bi_2WO_6 has less photocatalytic activity due to its high recombination of photogenerated carriers. Hence, UV-light of 365 nm was used in this study to get better catalytic efficiency of the synthesized catalysts towards the reduction of 4-NP to 4-AP. Fig. 9a shows the UV-visible spectra of 4-NP and 4-AP at a concentration of 0.0001 M. The peak around 400 nm is the prominent peak of 4-nitrophenol and the peak at 316 nm corresponds to the 4-AP. Fig. S11† shows the UV-visible spectrum of 4-NP at various concentration. It is observed that all concentrations below 1×10^{-3} M give an absorbance less than 1. So the concentration of 4-NP was fixed as 0.0001 M for initial studies. All controlled experiments with the conditions (1) 4-NP + dark condition, (2) 4-NP + $NaBH_4$ + dark condition, (3) 4-NP + $NaBH_4$ + dark condition + Bi_2WO_6/rGO/$SnFe_2O_4$ and (4) 4-NP + $NaBH_4$ + Bi_2WO_6/rGO/$SnFe_2O_4$ + light were done to know the best reduction condition (Fig. 9b). The combination of 4-NP + $NaBH_4$ + Bi_2WO_6/rGO/$SnFe_2O_4$ + light showed the best catalytic reduction property with an increased absorbance peak of 4-AP at 316 nm in UV-Vis spectrogram (Fig. 9c) and thus it was fixed as the reduction condition throughout the experiment. The photocatalytic reduction of 4-NP to 4-AP was also carried out with $SnFe_2O_4$, rGO-$SnFe_2O_4$, Bi_2WO_6, rGO/Bi_2WO_6, and Bi_2WO_6/$SnFe_2O_4$ individually under UV-light irradiation in the presence of $NaBH_4$. Different parameters such as concentration of 4-NP, the dosage of catalyst, time, and pH of the mixture prepared were optimised for each catalyst prepared. Fig. S12–S16† shows the photocatalytic reduction efficiency of each catalyst under optimised parameters for 90 min in the presence of $NaBH_4$ and light. The optimised parameters were 1×10^{-3} M of 4-NP as concentration, 10 mg of catalyst prepared, and pH of 7 for time duration of 90 min. The colour of the mixture was pale yellow initially and it changed to intense yellow colour after 50 min. This intense yellow colour indicates the formation of a 4-nitrophenolate ion, but the reaction mixture turned almost colourless in the presence of ternary nanocomposite Bi_2WO_6/rGO/$SnFe_2O_4$ catalyst after 90 min. The reaction with Bi_2WO_6/rGO/$SnFe_2O_4$ followed

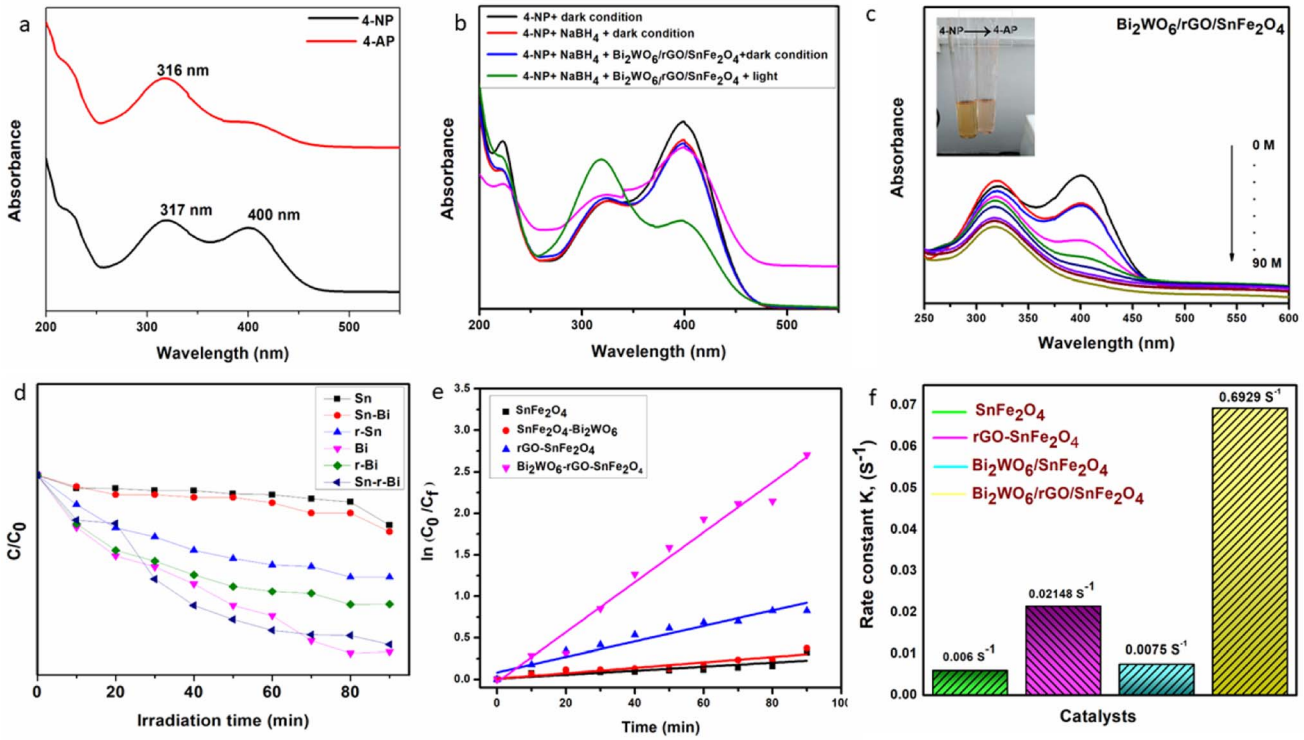

Fig. 9 (a) UV-Vis spectrum of 4-NP and 4-AP, (b) UV-Vis spectrum of 4-NP reduction during various conditions, (c) UV-Vis spectrum of 4-NP photocatalytic reduction to 4-AP using Bi_2WO_6/rGO/$SnFe_2O_4$, (d and e) kinetics plot, (f) bar graph showing the various rate constants of first order kinetics.

pseudo-first-order kinetics with R^2 value of near to 1. Also in photocatalytic reduction of 4-NP to 4-AP (Fig. 9d–e) using $NaBH_4$ as a reducing agent, the concentration of $NaBH_4$ was very high in comparison to 4-NP which can be considered negligible and remains constant.[49] The reaction rate constant (K) is higher for the ternary nanocomposite Bi_2WO_6/rGO/$SnFe_2O_4$ (Fig. 9f). All results suggest that ternary nanocomposite Bi_2WO_6/rGO/$SnFe_2O_4$ has better catalytic property towards 4-NP reduction to 4-AP in the presence of light and $NaBH_4$.

5.10 Stability of the catalyst

Recyclability and reusability is one of the factors to be considered for the synthesised catalyst. The stability of the final ternary nanocomposites (Bi_2WO_6/rGO/$SnFe_2O_4$) was carried out under the optimized experimental conditions. The photocatalytic reduction efficiency was done for 6 consecutive cycles (Fig. 10). The time taken for the reduction increased after each recycling process, but no change in the XRD pattern of the recycled catalyst was noticed after 6 consecutive cycles (Fig. S17†) which clearly shows that no structural damage happened to the catalyst during the experimental conditions.

5.11 Possible reduction mechanism

(a) In the presence of $NaBH_4$

The aqueous solution of 4-NP is a pale yellow solution having an absorption peak at 316 nm, but it turns to a deep yellow solution in the presence of excess $NaBH_4$ solution with a λ_{max} of 400 nm due to the formation of 4-nitrophenolate ions in the control experiment[52–56] (Fig. S18†). In the presence of UV-irradiation and $NaBH_4$ there was no reduction of 4-NP to 4-AP due to the high kinetic barrier among the two negatively charged species, but in the presence of nanocomposites, the electrons from the nucleophile borohydride ions (BH_4^-) migrate to rGO *via* semiconductor heterojunction

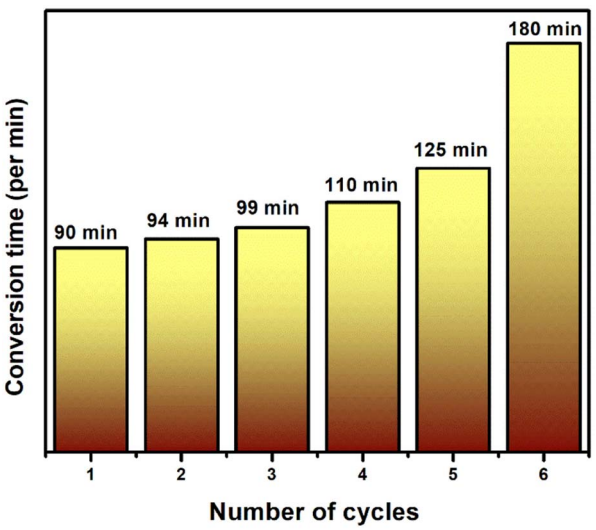

Fig. 10 Catalytic stability of Bi_2WO_6/rGO/$SnFe_2O_4$ for 6 successive cycles.

nanocomposites where rGO behaves as an electrons sink.[57,58] Simultaneously, BH_4^- ions generates H_2 in an aqueous medium which forms metal hydride on the surface of nanocomposites. Now, 4-NP is adsorbed on the catalyst surface and generates a nanocomposite-4-nitrophenolate intermediate with H-bonding to oxygen atoms of nitrate ions which is further reduced to nitroso group (NO) and diffused out from the surface. Further, nitroso compounds are adsorbed onto the catalyst surface and form an H-bonding with the O-atom of the NO group as well N-atom of the NO group which on reduction forms hydroxylamine (NHOH). Finally, one hydride ion attacks the N-atom of the NHOH group and forms the final reduced product of 4-AP. Given below is the scheme of possible mechanism for the photocatalytic reduction of 4-NP to 4-AP in the presence of $NaBH_4$ with a photocatalyst (Scheme 2).[59–62]

Scavenging studies were done to know the reactive oxygen species that could be responsible for the photocatalytic activity of the catalyst without reducing agents. EDTA, IPA, $AgNO_3$, and benzoquinone were used as the radical trapping agents. Fig. 11 shows the photocatalytic efficiency of 4-NP with catalyst and radical trapping agents without $NaBH_4$ in the presence of light. The role of h^+ was found using EDTA and it shows an efficiency of 18.9%. Electron (e^-) influence was determined by the addition of $AgNO_3$ and it shows an efficiency of 42.72%. The reaction using IPA and benzoquinone shows the role of ^-OH and superoxides. These results prove that Bi_2WO_6/rGO/$SnFe_2O_4$ can be used as an effective photocatalyst for degradation dyes and other toxic compounds in the presence of light.

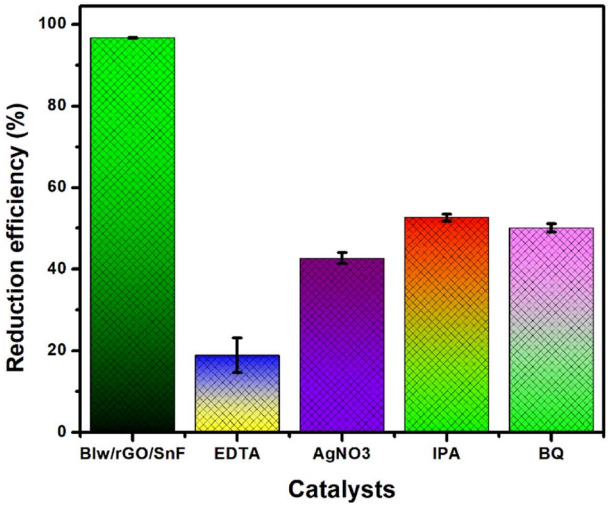

Fig. 11 Photoreduction efficiency of type-II ternary Bi_2WO_6/rGO/$SnFe_2O_4$ heterojunction nanocomposite in the presence of different radical trapping agents.

Table 3 summarizes some of the reported works related to 4-NP reduction to 4-AP reduction in the presence of $NaBH_4$ without light. All the reported studies mentioned the complete

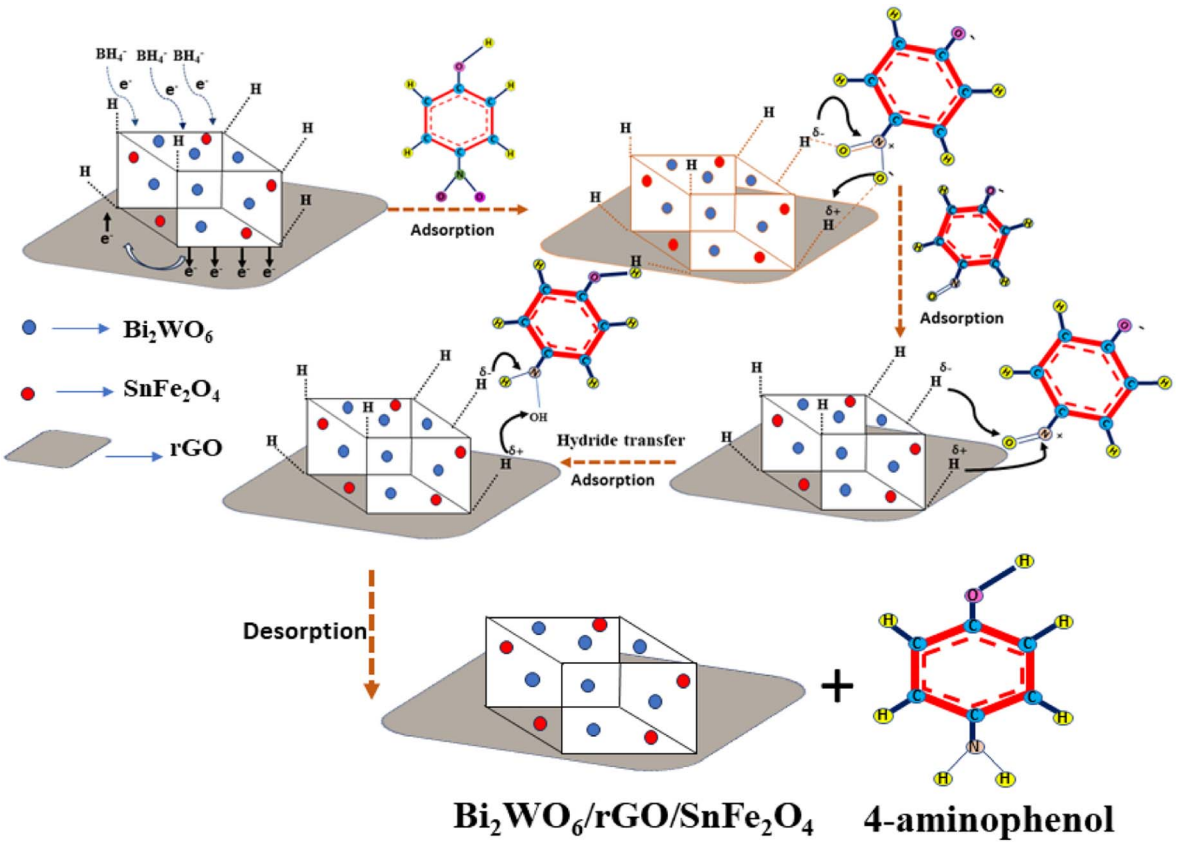

Scheme 2 Plausible mechanism for the photocatalytic reduction of 4-NP to 4-AP using Bi_2WO_6/rGO/$SnFe_2O_4$.

Table 3 Reported literature on the reduction of 4-nitrophenol to 4-aminophenol

Material	Synthesis method	Time duration (min)	% of reduction	References
$BaWO_4$/NRGO-*g*-C_3N_4	One pot microwave	60	~100	63
$NiWO_4$–ZnO–NRGO	Microwave irradiation	100	~100	64
RGO–Fe_2WO_4/Fe_3O_4	Microwave	45	~100	65
Cu_xNi_{100-x}–CeO_2	Liquid impregnation	25	~100	66
Pt–Ni/TiO_2	Electrospinning	45	~100	67
NRGO–$CoWO_4$–Fe_2O_3	Microwave	30	~100	68
Bi_2WO_6/rGO/$SnFe_2O_4$	Hydrothermal	90	~100	This study

reduction of 4-NP to 4-AP within 100 min.[63–68] Our study also noticed complete reduction of 4-NP to 4-AP within 90 min. This work would be more helpful in the future aspect due to the increase in amount of 4-NP in the water bodies day by day. Moreover the synthesised catalyst can be easily used for other environmental remediations like removal of harmful substances as well as detections of substances through sensing which would be a help in waste water treatment and policy makers.

6. Conclusion

In summary, Bi_2WO_6/rGO/$SnFe_2O_4$ spinel based heterojunction nanocomposite was synthesised *via* hydrothermal method. The prepared heterostructure nanocomposite was characterized using XRD, FT-IR, UV-DRS, FESEM, BET, Raman spectroscopy, and XPS. Individual composites $SnFe_2O_4$, rGO/$SnFe_2O_4$, Bi_2WO_6, rGO/Bi_2WO_6 Bi_2WO_6/$SnFe_2O_4$ were also separately synthesised for comparative studies and characterized. A simple model study of reduction of 4-NP to 4-AP using $NaBH_4$ in the presence of light was carried out to understand the catalytic efficiency of the synthesised catalysts. The final ternary nanocomposite showed a better photocatalytic reduction efficiency of 96% with pseudo-first order kinetics and an R^2 value of 0.97961. The scavenging study results suggest the degradation efficiency of Bi_2WO_6/rGO/$SnFe_2O_4$ which could be utilised for further degradation of dyes or organic compounds. Thus, a highly efficient spinel-based ternary nanocomposite was synthesised with good catalytic properties which could be used for many applications, especially for environmental remediation studies.

Ethical statement

Research involving no human participants and/or animals.

Author contributions

All authors contributed to the study conception and design. Material preparation, data collection and analysis were performed by [VN] and [BKM]. The first draft of the manuscript was written by [VN] and all authors commented on previous versions of the manuscript. All authors read and approved the final manuscript.

Conflicts of interest

The authors declare that they have no conflict of interest.

Acknowledgements

The authors take this opportunity to express their gratitude to the Vellore Institute of Technology, Vellore for providing all the financial support, a workplace, and instrumental assistance for this study to be completed. The authors acknowledge the help of SAS-SIF for the characterization of the synthesized nanocomposites. Also, the authors deeply acknowledge SAIF-IITM for providing Raman spectroscopy and HR-TEM and also IISER-Trivandrum for XPS analysis of the synthesized nanocomposites.

References

1 V. S. Kiran and S. Sumathi, Comparison of catalytic activity of bismuth substituted cobalt ferrite nanoparticles synthesized by combustion and co-precipitation method, *J. Magn. Magn. Mater.*, 2017, **421**, 113–119, DOI: 10.1016/j.jmmm.2016.07.068.

2 J. C. Spain and D. T. Gibson, Pathway for biodegradation of para-nitrophenol in a Moraxella sp, *Appl. Environ. Microbiol.*, 1991, **57**(3), 812–819, DOI: 10.1128/aem.57.3.812-819.1991.

3 Z. Liu, C. Yang and C. Qiao, Biodegradation of p-nitrophenol and 4-chlorophenol by Stenotrophomonas sp, *FEMS Microbiol. Lett.*, 2007, **277**(2), 150–156, DOI: 10.1111/j.1574-6968.2007.00940.x.

4 J. R. Chiou, B. H. Lai, K. C. Hsu and D. H. Chen, One-pot green synthesis of silver/iron oxide composite nanoparticles for 4-nitrophenol reduction, *J. Hazard. Mater.*, 2013, **248**, 394–400, DOI: 10.1016/j.jhazmat.2013.01.030.

5 M. S. Samuel, A. Sivaramakrishna and A. Mehta, Bioremediation of p-Nitrophenol by Pseudomonas putida 1274 strain, *J. Environ. Health Sci. Eng.*, 2014, **12**, 1–8, DOI: 10.1186/2052-336X-12-53.

6 J. Feng, L. Su, Y. Ma, C. Ren, Q. Guo and X. Chen, $CuFe_2O_4$ magnetic nanoparticles: A simple and efficient catalyst for the reduction of nitrophenol, *Chem. Eng. J.*, 2013, **221**, 16–24, DOI: 10.1016/j.cej.2013.02.009.

7 M. P. Reddy and A. M. A. Mohamed, One-pot solvothermal synthesis and performance of mesoporous magnetic ferrite MFe_2O_4 nanospheres, *Microporous Mesoporous Mater.*, 2015, **215**, 37–45, DOI: 10.1016/j.micromeso.2015.05.024.

8 Y. Liu, L. Zhou, Y. Hu, C. Guo, H. Qian, F. Zhang and X. W. D. Lou, Magnetic-field induced formation of 1D Fe_3O_4/C/CdS coaxial nanochains as highly efficient and reusable photocatalysts for water treatment, *J. Mater. Chem.*, 2011, **21**(45), 18359–18364, DOI: 10.1039/C1JM13789A.

9 Y. Wang, J. Ning, E. Hu, C. Zheng, Y. Zhong and Y. Hu, Direct coating ZnO nanocrystals onto 1D Fe_3O_4/C composite microrods as highly efficient and reusable photocatalysts for water treatment, *J. Alloys Compd.*, 2015, **637**, 301–307, DOI: 10.1016/j.jallcom.2015.03.033.

10 Z. Zhu, X. Li, Q. Zhao, Y. Shi, H. Li and G. Chen, Surface photovoltage properties and photocatalytic activities of nanocrystalline $CoFe_2O_4$ particles with porous superstructure fabricated by a modified chemical coprecipitation method, *J. Nanopart. Res.*, 2011, **13**, 2147–2155, DOI: 10.1007/s11051-010-9973-7.

11 L. Han, X. Zhou, L. Wan, Y. Deng and S. Zhan, Synthesis of $ZnFe_2O_4$ nanoplates by succinic acid-assisted hydrothermal route and their photocatalytic degradation of rhodamine B under visible light, *J. Environ. Chem. Eng.*, 2014, **2**(1), 123–130, DOI: 10.1016/j.jece.2013.11.031.

12 Y. Shen, L. Wang, Y. Wu, X. Li, Q. Zhao, Y. Hou and W. Teng, Facile solvothermal synthesis of $MnFe_2O_4$ hollow nanospheres and their photocatalytic degradation of benzene investigated by in situ FTIR, *Catal. Commun.*, 2015, **68**, 11–14, DOI: 10.1016/j.catcom.2015.04.025.

13 P. Xiong, Y. Fu, L. Wang and X. Wang, Multi-walled carbon nanotubes supported nickel ferrite: A magnetically recyclable photocatalyst with high photocatalytic activity on degradation of phenols, *Chem. Eng. J.*, 2012, **195**, 149–157, DOI: 10.1016/j.cej.2012.05.007.

14 R. K. Gupta, K. Ghosh and P. K. Kahol, Structural and magnetic properties of epitaxial $SnFe_2O_4$ thin films, *Mater. Lett.*, 2011, **65**(14), 2149–2151. 10.1016/j.matlet.2011.04.059.

15 Q. Mahmood, B. U. Haq, M. Rashid, N. A. Noor, S. AlFaify and A. Laref, First-principles study of magnetic and thermoelectric properties of $SnFe_2O_4$ and $SnCo_2O_4$ spinels, *J. Solid State Chem.*, 2020, **286**, 121279. 10.1016/j.jssc.2020.121279.

16 A. Soufi, H. Hajjaoui, R. Elmoubarki, M. Abdennouri, S. Qourzal and N. Barka, spinel ferrites nanoparticles: synthesis methods and application in heterogeneous fenton oxidation of organic pollutants–a review, *Appl. Surf. Sci. Adv.*, 2021, **6**, 100145. 10.1016/j.apsadv.2021.100145.

17 S. Yao, J. Wei, B. Huang, S. Feng, X. Zhang, X. Qin and J. Zhan, Morphology modulated growth of bismuth tungsten oxide nanocrystals, *J. Solid State Chem.*, 2009, **182**(2), 236–239. 10.1016/j.jssc.2008.09.016.

18 Y. Sun, B. Qu, Q. Liu, S. Gao, Z. Yan, W. Yan and Y. Xie, Highly efficient visible-light-driven photocatalytic activities in synthetic ordered monoclinic $BiVO_4$ quantum tubes–graphene nanocomposites, *Nanoscale*, 2012, **4**(12), 3761–3767. 10.1039/C2NR30371J.

19 L. Zhang, H. Wang, Z. Chen, P. K. Wong and J. Liu, Bi_2WO_6 micro/nano-structures: synthesis, modifications and visible-light-driven photocatalytic applications, *Appl. Catal., B*, 2011, **106**(1–2), 1–13, DOI: 10.1016/j.apcatb.2011.05.008.

20 H. Cheng, B. Huang, Y. Dai, X. Qin, X. Zhang, Z. Wang and M. Jiang, Visible-light photocatalytic activity of the metastable $Bi_{20}TiO_{32}$ synthesized by a high-temperature quenching method, *J. Solid State Chem.*, 2009, **182**(8), 2274–2278, DOI: 10.1016/j.jssc.2009.06.006.

21 L. Zhang and Y. Zhu, A review of controllable synthesis and enhancement of performances of bismuth tungstate visible-light-driven photocatalysts, *Catal. Sci. Technol.*, 2012, **2**(4), 694–706, DOI: 10.1039/C2CY00411A.

22 H. Takeda, T. Nishida, S. Okamura and T. Shiosaki, Crystal growth of bismuth tungstate Bi_2WO_6 by slow cooling method using borate fluxes, *J. Eur. Ceram. Soc.*, 2005, **25**(12), 2731–2734, DOI: 10.1016/j.jeurceramsoc.2005.03.184.

23 M. Hamada, H. Tabata and T. Kawai, Microstructure and dielectric properties of epitaxial Bi_2WO_6 deposited by pulsed laser ablation, *Thin Solid Films*, 1997, **306**(1), 6–9, DOI: 10.1016/S0040-6090(97)00244-7.

24 S. Shamaila, A. K. L. Sajjad, F. Chen and J. Zhang, Study on highly visible light active Bi_2O_3 loaded ordered mesoporous titania, *Appl. Catal., B*, 2010, **94**(3–4), 272–280, DOI: 10.1016/j.apcatb.2009.12.001.

25 J. Ren, W. Wang, S. Sun, L. Zhang and J. Chang, Enhanced photocatalytic activity of Bi_2WO_6 loaded with Ag nanoparticles under visible light irradiation, *Appl. Catal., B*, 2009, **92**(1–2), 50–55. 10.1016/j.apcatb.2009.07.022.

26 F. Ren, J. Zhang, Y. Wang and W. Yao, A graphene-coupled Bi_2WO_6 nanocomposite with enhanced photocatalytic performance: a first-principles study, *Phys. Chem. Chem. Phys.*, 2016, **18**(20), 14113–14121. 10.1039/C6CP00458J.

27 S. P. Lonkar, V. V. Pillai and S. M. Alhassan, Facile and scalable production of heterostructured ZnS-ZnO/Graphene nano-photocatalysts for environmental remediation, *Sci. Rep.*, 2018, **8**, 13401. 10.1038/s41598-018-31539-7.

28 M. M. J. Sadiq, U. Sandhya Shenoy and D. Krishna Bhat, Novel RGO–$ZnWO_4$–Fe_3O_4 nanocomposite as high performance visible light photocatalyst, *RSC Adv.*, 2016, **6**(66), 61821–61829. 10.1039/C6RA13002J.

29 M. Mohamed Jaffer Sadiq and K. Krishna Bhat, Novel RGO-$ZnWO_4$-Fe_3O_4 nanocomposite as an efficient catalyst for rapid reduction of 4-nitrophenol to 4-aminophenol, *Ind. Eng. Chem. Res.*, 2016, **55**(27), 7267–7272, DOI: 10.1021/acs.iecr.6b01882.

30 B. Paulchamy, G. Arthi and B. D. Lignesh, A simple approach to stepwise synthesis of graphene oxide nanomaterial, *J. Nanomed. Nanotechnol.*, 2015, **6**(1), 1, DOI: 10.4172/2157-7439.1000253.

31 Y. H. Sun, M. X. Huang, D. C. Guan, G. L. Zhang, J. L. Wei, J. M. Nan and F. Y. Yi, Influence of the Sn(Fe)–C bonds content in $SnFe_2O_4$@reduced graphene oxide composites on the electrochemical behavior of lithium-ion batteries, *J.*

Alloys Compd., 2021, **854**, 157297, DOI: 10.1016/j.jallcom.2020.157297.

32 B. D. Cullity, *Elements of X-ray Diffraction*, Addison-Wesley Publishing, 1956.

33 T. R. Tatarchuk, N. D. Paliychuk, M. Bououdina, B. Al-Najar, M. Pacia, W. Macyk and A. Shyichuk, Effect of cobalt substitution on structural, elastic, magnetic and optical properties of zinc ferrite nanoparticles, *J. Alloys Compd.*, 2018, **731**, 1256–1266, DOI: 10.1016/j.jallcom.2017.10.103.

34 G. Pandey and S. Dixit, Growth mechanism and optical properties determination of CdS nanostructures, *J. Phys. Chem. C*, 2011, **115**(36), 17633–17642, DOI: 10.1021/jp2015897.

35 S. P. Dubey, T. T. Nguyen, Y. N. Kwon and C. Lee, Synthesis and characterization of metal-doped reduced graphene oxide composites, and their application in removal of Escherichia coli, arsenic and 4-nitrophenol, *J. Ind. Eng. Chem.*, 2015, **29**, 282–288, DOI: 10.1016/j.jiec.2015.04.008.

36 S. Stankovich, D. A. Dikin, R. D. Piner, K. A. Kohlhaas, A. Kleinhammes, Y. Jia and R. S. Ruoff, Synthesis of graphene-based nanosheets via chemical reduction of exfoliated graphite oxide, *Carbon*, 2007, **45**(7), 1558–1565, DOI: 10.1016/j.carbon.2007.02.034.

37 Y. Zhang, L. Xiao, K. Xu, J. Song and F. Zhao, Graphene oxide-enveloped Bi_2WO_6 composites as a highly efficient catalyst for the thermal decomposition of cyclotrimethylenetrinitramine, *RSC Adv.*, 2016, **6**(48), 42428–42434, DOI: 10.1039/C6RA05042E.

38 G. Kumar and R. K. Dutta, Fabrication of plate-on-plate SnS2/Bi2WO6 nanocomposite as photocatalyst for sunlight mediated degradation of antibiotics in aqueous medium, *J. Phys. Chem. Solids*, 2022, **164**, 110639, DOI: 10.1016/j.jpcs.2022.110639.

39 C. Lu, D. Yang, L. Wang, S. Wen, D. Cao, C. Tu and W. Huang, Facile construction of CoO/Bi2WO6 pn heterojunction with following Z-Scheme pathways for simultaneous elimination of tetracycline and Cr(VI) under visible light irradiation, *J. Alloys Compd.*, 2022, **904**, 164046, DOI: 10.1016/j.jpcs.2022.110639.

40 B. Li, C. Lai, G. Zeng, L. Qin, H. Yi, D. Huang and S. Liu, Facile hydrothermal synthesis of Z-scheme $Bi_2Fe_4O_9$/Bi_2WO_6 heterojunction photocatalyst with enhanced visible light photocatalytic activity, *ACS Appl. Mater. Interfaces*, 2018, **10**(22), 18824–18836, DOI: 10.1021/acsami.8b06128.

41 Y. Jia, Q. Wang, W. Zhang, M. Kang, J. S. Bae and C. Liu, Octahedron-shaped $SnFe_2O_4$ for boosting photocatalytic degradation and CO_2 reduction, *J. Alloys Compd.*, 2021, **889**, 161737, DOI: 10.1016/j.jallcom.2021.161737.

42 P. Tan, Active phase, catalytic activity, and induction period of Fe/zeolite material in nonoxidative aromatization of methane, *J. Catal.*, 2016, **338**, 21–29, DOI: 10.1016/j.jcat.2016.01.027.

43 X. Duan, K. O'Donnell, H. Sun, Y. Wang and S. Wang, Sulfur and nitrogen co-doped graphene for metal-free catalytic oxidation reactions, *Small*, 2015, **11**(25), 3036–3044, DOI: 10.1002/smll.201403715.

44 S. Majumdar, P. Nag and P. S. Devi, Enhanced performance of CNT/SnO_2 thick film gas sensors towards hydrogen, *Mater. Chem. Phys.*, 2014, **147**(1–2), 79–85, DOI: 10.1016/j.matchemphys.2014.04.009.

45 Y. Zhou, E. Antonova, Y. Lin, J. D. Grunwaldt, W. Bensch and G. R. Patzke, In Situ X-ray Absorption Spectroscopy/Energy-Dispersive X-ray Diffraction Studies on the Hydrothermal Formation of $Bi_2W_{1-x}Mo_xO_6$ Nanomaterials, *Eur. J. Inorg. Chem.*, 2012, **2012**(5), 783–789, DOI: 10.1002/ejic.201101116.

46 R. Wang, Z. Jiang, L. Xu and C. Liu, Synthesis of Dy(III) doped Bi_2WO_6 photocatalyst with highly efficient photocatalytic performance under simulated sunlight, *J. Mater. Sci.: Mater. Electron.*, 2021, **32**, 6931–6941, DOI: 10.1007/s10854-021-05399-3.

47 J. N. Coleman, M. Lotya, A. O'Neill, S. D. Bergin, P. J. King, U. Khan and V. Nicolosi, Two-dimensional nanosheets produced by liquid exfoliation of layered materials, *Science*, 2011, **331**(6017), 568–571, DOI: 10.1126/science.1194975.

48 Y. H. Sun, M. X. Huang, D. C. Guan, G. L. Zhang, J. L. Wei, J. M. Nan and F. Y. Yi, Influence of the Sn(Fe)–C bonds content in $SnFe_2O_4$@reduced graphene oxide composites on the electrochemical behavior of lithium-ion batteries, *J. Alloys Compd.*, 2021, **854**, 157297, DOI: 10.1016/j.jallcom.2020.157297.

49 Z. Chen, S. Liu, M. Q. Yang and Y. J. Xu, Synthesis of uniform CdS nanospheres/graphene hybrid nanocomposites and their application as visible light photocatalyst for selective reduction of nitro organics in water, *ACS Appl. Mater. Interfaces*, 2013, **5**(10), 4309–4319, DOI: 10.1021/am4010286.

50 *Toxicological Profile for Nitrophenols, Agency for Toxic Substances and Disease Registry*, U.S. Public Health Service, 1992.

51 U.S. EPA (U.S. Environmental Protection Agency), *Provisional Peer Reviewed Toxicity Values for p-aminophenol* (CASRN 123-30-8) [EPA Report], Cincinnati, OH, 2005.

52 A. Hatamifard, M. Nasrollahzadeh and S. M. Sajadi, Biosynthesis, characterization and catalytic activity of an Ag/zeolite nanocomposite for base- and ligand-free oxidative hydroxylation of phenylboronic acid and reduction of a variety of dyes at room temperature, *New J. Chem.*, 2016, **40**, 2501–2513, DOI: 10.1039/C5NJ02909K.

53 M. Nasrollahzadeh, M. Sajjadi, M. Maham, S. M. Sajadi and A. A. Barzinjy, Biosynthesis of the palladium/sodium borosilicate nanocomposite using Euphorbia milii extract and evaluation of its catalytic activity in the reduction of chromium (VI), nitro compounds and organic dyes, *Mater. Res. Bull.*, 2018, **102**, 24–35, DOI: 10.1016/j.materresbull.2018.01.032.

54 M. Khazaei, A. Khazaei, M. Nasrollahzadeh and M. R. Tahsili, Highly efficient reusable Pd nanoparticles based on eggshell: green synthesis, characterization and their application in catalytic reduction of variety of organic dyes and ligand-free oxidative hydroxylation of phenylboronic acid at room temperature, *Tetrahedron*, 2017, **73**, 5613–5623, DOI: 10.1016/j.tet.2017.04.016.

55 B. Li, Y. Hao, X. Shao, H. Tang, T. Wang, J. Zhu and S. Yan, Synthesis of hierarchically porous metal oxides and Au/TiO_2 nanohybrids for photodegradation of organic dye and catalytic reduction of 4-nitrophenol, *J. Catal.*, 2015, **329**, 368–378, DOI: **10.1016/j.jcat.2015.05.015**.

56 S. Wang, B. Y. Guan, X. Wang and X. W. D. Lou, Formation of hierarchical Co9S8@ZnIn2S4 heterostructured cages as an efficient photocatalyst for hydrogen evolution, *J. Am. Chem. Soc.*, 2018, **140**(45), 15145–15148, DOI: **10.1016/j.jcat.2015.05.015**.

57 X. Yang, Y. Li, P. Zhang, R. Zhou, H. Peng, D. Liu and J. Gui, Photoinduced in situ deposition of uniform and well-dispersed PtO2 nanoparticles on ZnO nanorods for efficient catalytic reduction of 4-nitrophenol, *ACS Appl. Mater. Interfaces*, 2018, **10**(27), 23154–23162, DOI: **10.1021/acsami.8b06815**.

58 G. Wu, X. Liang, L. Zhang, Z. Tang, M. Al-Mamun, H. Zhao and X. Su, Fabrication of Highly Stable Metal Oxide Hollow Nanospheres and Their Catalytic Activity toward 4-Nitrophenol Reduction, *ACS Appl. Mater. Interfaces*, 2017, **9**, 18207–18214, DOI: **10.1021/acsami.7b03120**.

59 M. Kohantorabi and M. R. Gholami, Fabrication of novel ternary Au/CeO_2@gC_3N_4 nanocomposite: kinetics and mechanism investigation of 4-nitrophenol reduction, and benzyl alcohol oxidation, *Appl. Phys. A: Mater. Sci. Process.*, 2018, **124**, 1–17, DOI: **10.1007/S00339-018-1858-0**.

60 X. Zhou, Y. Li, Y. Xing, X. Liu, X. Yu and Y. Yu, Comparison of the catalytic properties of Au nanoparticles supported on different two-dimensional carriers, *J. Phys. Chem. Solids*, 2020, **142**, 109438, DOI: **10.1016/j.jpcs.2020.109438**.

61 X. Zhang, X. He, Z. Kang, M. Cui, D. P. Yang and R. Luque, Waste eggshell-derived dual-functional CuO/ZnO/eggshell nanocomposites: (Photo) catalytic reduction and bacterial inactivation, *ACS Sustainable Chem. Eng.*, 2019, **7**(18), 15762–15771, DOI: **10.1021/acssuschemeng.9b04083**.

62 S. Manivannan, S. An, J. Jeong, M. Viji and K. Kim, Hematite/M (M = Au, Pd) catalysts derived from a double-hollow Prussian blue microstructure: simultaneous catalytic reduction of o-and p-nitrophenols, *ACS Appl. Mater. Interfaces*, 2020, **12**(15), 17557–17570, DOI: **10.1021/acsami.0c01704**.

63 M. M. J. Sadiq, U. S. Shenoy and D. K. Bhat, Synthesis of $BaWO_4$/NRGO-gC_3N_4 nanocomposites with excellent multifunctional catalytic performance via microwave approach, *Front. Mater. Sci.*, 2018, **12**, 247–263, DOI: **10.1007/s11706-018-0433-0**.

64 M. M. J. Sadiq, U. S. Shenoy and D. K. Bhat, $NiWO_4$-ZnO-NRGO ternary nanocomposite as an efficient photocatalyst for degradation of methylene blue and reduction of 4-nitro phenol, *J. Phys. Chem. Solids*, 2017, **109**, 124–133, DOI: **10.1016/j.jpcs.2017.05.023**.

65 M. M. J. Sadiq, U. S. Shenoy and D. K. Bhat, Enhanced photocatalytic performance of N-doped RGO-$FeWO_4$/Fe_3O_4 ternary nanocomposite in environmental applications, *Mater. Today Chem.*, 2017, **4**, 133–141. **https://idr.nitk.ac.in/jspui/handle/123456789/11474**.

66 M. Kohantorabi and M. R. Gholami, Kinetic analysis of the reduction of 4-nitrophenol catalyzed by CeO_2 nanorods-supported CuNi nanoparticles, *Ind. Eng. Chem. Res.*, 2017, **56**(5), 1159–1167, DOI: **10.1021/acs.iecr.6b04208**.

67 A. Celebioglu, K. S. Ranjith, H. Eren, N. Biyikli and T. Uyar, Surface decoration of Pt nanoparticles via ALD with TiO_2 protective layer on polymeric nanofibers as flexible and reusable heterogeneous nanocatalysts, *Sci. Rep.*, 2017, **7**(1), 13401, DOI: **10.1038/s41598-017-13805-2**.

68 M. Mohamed Jaffer Sadiq, U. Sandhya Shenoy and D. Krishna Bhat, Novel NRGO-$CoWO_4$-Fe_2O_3 nanocomposite as an efficient catalyst for dye degradation and reduction of 4-nitrophenol, *Mater. Chem. Phys.*, 2018, **208**, 112–122, DOI: **10.1016/j.matchemphys.2018.01.012**.